Real-Time Capacity Estimation of Lithium-Ion Batteries Utilizing Thermal Dynamics

Dong Zhang, Satadru Dey, Hector E. Perez, *Member, IEEE*, and Scott J. Moura, *Member, IEEE*

***Abstract*— Increasing longevity remains one of the open challenges for Lithium-ion (Li-ion) battery technology. We envision a health-conscious advanced battery management system, which implements monitoring and control algorithms that increase battery lifetime while maintaining performance. For such algorithms, real-time battery capacity estimates are crucial. In this paper, we present an online capacity estimation scheme for Li-ion batteries. The key novelty lies in: 1) leveraging thermal dynamics to estimate battery capacity and 2) developing a hierarchical estimation algorithm with provable convergence properties. The algorithm consists of two stages working in cascade. The first stage estimates battery core temperature and heat generation based on a two-state thermal model, and the second stage receives the core temperature and heat generation estimation to estimate state-of-charge and capacity. Results from numerical simulations and experimental data illustrate the performance of the proposed capacity estimation scheme.**

***Index Terms*— Li-ion batteries, nonlinear estimation theory, real-time capacity estimation.**

I. Introduction

With the rapid evolution of smart grid technologies and electrified vehicles, the Lithium-ion (Li-ion) battery has become a prominent device for energy storage. An advanced battery management system (BMS) implements real-time control/estimation algorithms that enhance battery performance while improving safety. A crucial function of a BMS is to estimate the state-of-charge (SOC) and the state-of-health (SOH). Capacity fade is one of the most important metrics among all of the principal effects of battery aging [1]. Accurate real-time capacity estimation with certified convergence properties is still an unsolved problem. In this paper, we propose and rigorously analyze a thermal model-based online capacity estimation scheme.

Manuscript received February 13, 2018; revised September 17, 2018; accepted November 25, 2018. Date of publication January 3, 2019; date of current version April 13, 2020. Manuscript received in final form December 3, 2018. This work was supported in part by the National Science Foundation under Grant 1408107 and in part by Robert Bosch RTC. Recommended by Associate Editor A. Serrani. *(Corresponding author: Dong Zhang.)*

D. Zhang and H. E. Perez are with the Department of Civil and Environmental Engineering, University of California at Berkeley, Berkeley, CA 94720 USA (e-mail: dongzhr@berkeley.edu; heperez@berkeley.edu).

S. Dey is with the Department of Electrical Engineering, University of Colorado Denver, Denver, CO 80204 USA (e-mail: satadru.dey@ucdenver.edu).

S. J. Moura is with the Department of Civil and Environmental Engineering, University of California, Berkeley, CA 94720 USA, and also with the Smart Grid and Renewable Energy Laboratory, Tsinghua-Berkeley Shenzhen Institute, Shenzhen 518055, China (e-mail: smoura@berkeley.edu).

Color versions of one or more of the figures in this article are available online at http://ieeexplore.ieee.org.

Digital Object Identifier 10.1109/TCST.2018.2885681

The existing literature contains several approaches to capacity estimation. Broadly, they can be categorized into offline and online approaches.

Offline approaches generally develop capacity estimation scheme in specific laboratory settings with access to large amounts of battery data under varying operating conditions [2]–[4]. However, the applicability of the offline approaches is limited due to the following reasons: 1) we have access to very limited amount of data and 2) battery degradation depends significantly on users, operating conditions, and so on. Therefore, a single offline capacity estimation scheme may not be sufficient for these cases.

Online capacity estimation methods operate on embedded BMS microcontrollers utilizing real-time measurements. Generally, online approaches are comparatively more challenging than their offline counterparts, due to the lack of measured information and limited computation power. Several studies have investigated this. Seminal work exploring combined SOC and model parameter estimation using Kalman filter (KF) were introduced in [5]. In [6], a dual sliding mode observer consists of a fast-paced and a slow-paced time-varying observer was presented for estimating the SOC and SOH of Li-PB batteries. Lin *et al.* [7] developed an adaptive observer based on online parameterization method for battery core temperature estimation and health monitoring. Electrochemical model-based battery aging studies provide a sharp understanding of the underlying physical and chemical processes occurring during battery utilizations. For instance, a reduced-order electrochemical model for a composite electrode battery combined with KF was utilized for a dual-observer design to estimate SOC and capacity [8]. Moura *et al.* [9] performed the combined SOC/SOH estimation based on single particle model (SPM) and the concept of backstepping state estimator for partial differential equations. Xing *et al.* [10] and Orchard *et al.* [11] used the particle filter for battery state of health estimation. Machine learning tools for SOH estimation are attracting extensive attention in recent years. For example, the support vector machine is commonly used as a regression tool for SOH estimation [12]. However, none of the aforementioned approaches explore battery capacity estimation from a thermal perspective. Moreover, only a few of these algorithms have proven convergence properties—a crucial requirement for ensuring reliable operation in real-world BMS. In this paper, we propose and rigorously analyze a capacity estimation scheme that utilizes battery thermal dynamics.

The results presented in this paper is a significant extension of our previous work [13]. The extensions include: 1) providing algorithm validation on experimental capacity fade data from a commercial battery cell; 2) analyzing observer convergence with modeling uncertainties; and 3) refining the estimation algorithm by adding a real-time thermal model parameter identification block.

The rest of this paper is organized as follows. Section II presents the battery electrical and thermal models. Section III examines the thermal model parameter identifiability, state estimation with unknown input, and sliding mode observers with convergence analysis. Section IV highlights the benefits of thermal model-based capacity estimation against electrical only estimation. Section V discusses the capacity estimation algorithm validation on simulation and experimental data. Conclusions are drawn in Section VI.

II. Battery Model

In this section, a coupled electro-thermal model is detailed for a cylindrical lithium-iron-phosphate battery cell (A123 ANR26650M1). The model utilizes a coulomb counting method to capture the dynamics of SOC and a two-state thermal model that predicts battery surface and core temperature.

A. Electrical Model

The SOC is computed via the coulomb counting method by integrating the applied current normalized by battery capacity over time. The dynamical equation is given by

$$\frac{d\mathrm{SOC}(t)}{dt} = -\frac{I(t)}{C_{\mathrm{bat}}} \tag{1}$$

where $I(t)$ is the input current, and we specify positive $I(t)$ for discharge and negative $I(t)$ for charge. Parameter C_{bat} is the battery charge capacity in ampere-second.

B. Thermal Model

We consider a two-state lumped thermal model for a cylindrical battery, adopted from [14]. This model assumes homogeniety along the cell's longitudinal axis. The model states are core temperature (T_c) and surface temperature (T_s)

$$C_c\frac{dT_c(t)}{dt} = \frac{T_s(t)-T_c(t)}{R_c} + \dot{Q}(t) + \nu_c(t) \tag{2}$$

$$C_s\frac{dT_s(t)}{dt} = \frac{T_f(t)-T_s(t)}{R_u} - \frac{T_s(t)-T_c(t)}{R_c} + \nu_s(t) \tag{3}$$

$$\dot{Q}(t) = I(t)\left[\mathrm{OCV}(\mathrm{SOC}(t)) - V_T(t) - T(t)\frac{dU}{dT}\right] \tag{4}$$

$$T(t) = \frac{1}{2}(T_s(t)+T_c(t)) \tag{5}$$

$$y(t) = T_s(t) + n(t) \tag{6}$$

where R_c, R_u, C_c, and C_s represent the heat conduction resistance, convection resistance, core heat capacity, and surface heat capacity, respectively. Symbol $\dot{Q}(t)$ is the internal heat generation. Heat generation from resistive dissipation and entropic heat are considered, where dU/dT is the entropic coefficient and $T(t)$ is the average of surface and core temperature [15]. V_T denotes the measureable terminal voltage, whereas OCV is the open-circuit voltage as a function of state of charge. We assume the coolant flow rate is constant and the ambient temperature T_f is nearly constant [16]. We also introduce bounded terms $\nu_c(t)$ and $\nu_s(t)$ to model the uncertainties in the thermal dynamics, where $\nu_c(t) \le \overline{\nu}_c$ and $\nu_s(t) \le \overline{\nu}_s$. Estimates of $\overline{\nu}_c$ and $\overline{\nu}_s$ can be found by comparing the open-loop thermal model output with the experimental data. Moreover, a time-varying but bounded measurement noise $n(t) \le \overline{n}$ is considered, with $\overline{n} > 0$.

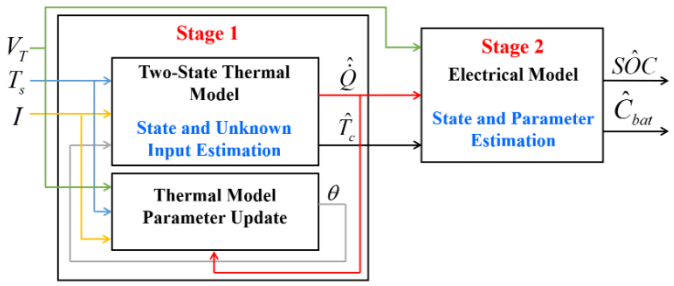

Fig. 1. Cascaded online capacity estimation structure.

Rearranging (2)–(6) into state-space form

$$\dot{x}(t) = Ax(t) + Bu(t) + G\dot{Q}(t) + \nu(t) \tag{7}$$

$$y(t) = Cx(t) + n(t) \tag{8}$$

where the input, states, and uncertainties are

$$u(t) = T_f, \quad x(t) = \begin{bmatrix} T_c(t) \\ T_s(t) \end{bmatrix}, \quad \nu(t) = \begin{bmatrix} \nu_c(t) \\ \nu_s(t) \end{bmatrix} < \overline{\nu} = \begin{bmatrix} \overline{\nu}_c \\ \overline{\nu}_s \end{bmatrix} \tag{9}$$

and the corresponding system matrices are

$$A = \begin{bmatrix} -\dfrac{1}{R_cC_c} & \dfrac{1}{R_cC_c} \\ \dfrac{1}{R_cC_s} & -\left(\dfrac{1}{R_uC_s} + \dfrac{1}{R_cC_s}\right) \end{bmatrix}, \quad B = \begin{bmatrix} 0 \\ \dfrac{1}{R_uC_s} \end{bmatrix}$$

$$G = \begin{bmatrix} \dfrac{1}{C_c} \\ 0 \end{bmatrix}, \quad C = \begin{bmatrix} 0 & 1 \end{bmatrix}. \tag{10}$$

Remark 1: The local observability of the thermal model (2)–(6) has been verified by computing the rank of the linearized system at the equilibrium points.

III. Online Capacity Estimation Scheme

We present a hierarchical structure depicted in Fig. 1. In Stage 1, heat generation $\dot{Q}$ in the T_c-dynamics (2) is treated as a bounded unknown input. An output error injection-based state and unknown input estimation technique, along with the two-state thermal model are employed to estimate the unmeasured state (T_c) and unmeasured input ($\dot{Q}$), using the online measurements of input current (I) and surface temperature (T_s). Based on the thermal model parameter sensitivity analysis, R_c is updated in real time to improve model and estimation accuracy. Next, the estimated core temperature $\widehat{T}_c$ and heat

generation $\widehat{\dot{Q}}$, as well as the measured terminal voltage (V_T), are utilized to algebraically compute a pseudomeasurement of OCV within Stage 2, where a sliding mode observer based on the SOC model is applied to simultaneously estimate the unmeasured state (SOC) and unknown parameter (C_{bat}). In Sections III-A and III-B, we detail the design of each stage.

A. Stage 1: Core Temperature and Heat Generation Estimation

The Stage 1 aims to estimate the core temperature (unmeasured state) and heat generation (unmeasured input).

1) Thermal Model Parameter Identification: We first evaluate the thermal parameter identifiability [17]. Consider the thermal model parameters

$$\theta_t = \begin{bmatrix} C_c & C_s & R_c & R_u \end{bmatrix}^\top. \tag{11}$$

The sensitivity vector

$$S = \begin{bmatrix} \dfrac{\partial y}{\partial C_c} & \dfrac{\partial y}{\partial C_s} & \dfrac{\partial y}{\partial R_c} & \dfrac{\partial y}{\partial R_u} \end{bmatrix} \in \mathbb{R}^{N\times 4} \tag{12}$$

represents each parameter's sensitivity in the output, where N is the number of measurements. The Gram–Schmidt orthonormalization of $S^\top S$ reveals information about linear dependence between parameters. Let $S^\top S = D^\top C D$ with $D \in \mathbb{R}^{4\times 4}$ and $C \in \mathbb{R}^{4\times 4}$, where $D(i,i) = \|S_i\|$ and $D(i,j) = 0$ for $i \neq j$, and $C(i,i) = 1$ and $C(i,j) = (\langle S_i, S_j\rangle / \|S_i\|\|S_j\|)$. Herein, $\|\cdot\|$ denotes the Euclidian norm and $\langle\cdot,\cdot\rangle$ is the inner product. Diagonal matrix D provides a quantification of parameter sensitivity. Strong linear dependence exists between $\theta_{t,i}$ and $\theta_{t,j}$ if the value of $(\langle S_i, S_j\rangle / \|S_i\|\|S_j\|)$ is near ± 1. This indicates that if the off-diagonal element of matrix C is near ± 1, then the corresponding pair of parameters are difficult to identify separately. An example of the thermal parameter sensitivity analysis based on the profile shown in Fig. 5 for a $LiFePO_4/LiC_6$ (LFP) cell is performed, and the result reveals that the model output is most sensitive to R_u (yet assumed to be constant in this paper) and R_c, and strong linear dependence exists between R_u, C_c, and R_c. Consequently, R_c is chosen to be identified in real time, considering parameter sensitivity and linear dependence.

Remark 2: According to [7], the heat capacities C_c and C_s are relatively constant over battery lifetime since they depend on the material thermal properties and the mass of the rolled electrode assembly and the casing. Meanwhile, R_u is affected by the coolant flow rate, which is assumed to be constant. Coincidently, the implication of sensitivity analysis matches the physical intuition, where the change of R_c over lifetime is the consequence of battery degradation.

An online parameter estimation algorithm, which aims to minimize the instantaneous squared error between measured surface temperature and model output by updating R_c, is running in real time to ensure estimation accuracy. A parametric model for such identification can be derived by performing

TABLE I
INITIAL THERMAL PARAMETERS FOR LFP CELL

C_c [J/K]	C_s [J/K]	R_c [K/W]	R_u [K/W]
59.5	4.4	1.61	3.14

Laplace Transformation on thermal model (2)–(3) [7]

$$\begin{aligned} s^2T_s - sT_{s,0} = {} & \frac{-1}{C_cC_sR_c}((C_c+C_s)sT_s - C_sT_{s,0} - C_cT_{c,0}) \\ & + \frac{1}{C_cC_sR_c}\widehat{\dot{Q}} + \frac{1}{C_cC_sR_cR_u}(T_f - T_s) \\ & + \frac{1}{C_sR_u}s(T_f - T_s) \end{aligned} \tag{13}$$

where $T_{s,0}$ and $T_{c,0}$ are the initial conditions of surface and core temperatures. Herein, note in (13) that we feedback the heat generation estimation from the upper block in Stage 1 to improve the estimates of thermal parameter, which is visualized by the red arrow in Fig. 1. It is assumed that battery evolves from the steady state, and thus $T_{s,0} = T_{c,0}$. Furthermore, the ambient temperature T_f is assumed to be constant, namely, $sT_f = 0$

$$\begin{aligned} & s^2T_s - sT_{s,0} + \frac{1}{C_sR_u}sT_s \\ & = \frac{1}{R_c}\left[-\frac{C_c+C_s}{C_cC_s}(sT_s - T_{s,0}) + \frac{1}{C_cC_s}\widehat{\dot{Q}} + \frac{1}{C_cC_sR_u}(T_f - T_s)\right]. \end{aligned} \tag{14}$$

For the parametric model in (14), let

$$\theta = \frac{1}{R_c} \tag{15}$$

$$Z(s) = s^2T_s - sT_{s,0} + \frac{1}{C_sR_u}sT_s \tag{16}$$

$$\Phi(s) = -\frac{C_c+C_s}{C_cC_s}(sT_s - T_{s,0}) + \frac{\widehat{\dot{Q}}}{C_cC_s} + \frac{T_f - T_s}{C_cC_sR_u} \tag{17}$$

yielding

$$Z(s) = \theta^\top \Phi(s). \tag{18}$$

The update law for $\hat{\theta}$ can be generated as follows:

$$\dot{\hat{\theta}} = \Gamma(Z - \hat{\theta}^\top\Phi)\Phi, \quad \hat{\theta}(0) = \hat{\theta}_0 \tag{19}$$

where $\Gamma = \Gamma^\top \succ 0$ is a symmetric positive-definite matrix that controls the convergence rate.

For the initial offline parameter identification for a fresh cell, particle swarm optimization (PSO) is employed to minimize the root-mean-squared error between the measured surface temperature and thermal model output. The initial thermal parameters identified by PSO are summarized in Table I.

2) Core Temperature and Heat Generation Estimation: We consider the following observer structure based on the thermal plant model (7) and (8):

$$\dot{\hat{x}}(t) = A\hat{x}(t) + Bu(t) + L[y(t) - \hat{y}(t)] \tag{20}$$

$$\hat{y}(t) = C\hat{x}(t) \tag{21}$$

where $\hat{x} = [\widehat{T}_c \ \ \widehat{T}_s]^\top$ denotes the estimated state vector, and $L = [L_1 \ \ L_2]^\top$, with $L_1, L_2 > 0$, is the observer gain vector to be designed. The following theorem provides the convergence results of the observer (20) and (21).

Theorem 3: Consider the locally observable thermal system (7) and (8) with bounded heat generation $|\dot{Q}(t)| \leq M_Q$, $\forall\, t \in \mathbb{R}^+$, and bounded model uncertainties $\nu < \overline{\nu}$, along with the observer (20) and (21). If there exists a gain matrix L and a positive definite matrix M such that

$$(A - LC)^\top + (A - LC) = -M \tag{22}$$

$$\lambda_{\min}(M)\|\tilde{x}(0)\| > 2(\overline{\Phi} + L\overline{n}) \tag{23}$$

then the state estimation error $\tilde{x}(t) = x(t) - \hat{x}(t)$ remains bounded in the following sense as $t \to \infty$:

$$\|\tilde{x}\| \leq R_b \triangleq \frac{2(\overline{\Phi} + L\overline{n})}{\lambda_{\min}(M)} \tag{24}$$

where $\overline{\Phi} = \|G\|M_Q + \|\overline{\nu}\|$ and $\lambda_{\min}(M)$ denotes the minimum eigenvalue of matrix M.

Theorem 3 leads to the notion of input-to-state stability (ISS) [18]. The proof for Theorem 3 is provided as follows.

Proof: Subtracting (20) from (7), the state estimation error dynamics can be written as

$$\begin{aligned}\dot{\tilde{x}}(t) = f(\tilde{x}) &= (A - LC)\tilde{x}(t) + G\dot{Q}(t) + \nu - Ln \\ &= (A - LC)\tilde{x}(t) + \Phi - Ln\end{aligned} \tag{25}$$

where $\Phi = G\dot{Q}(t) + \nu$, and let $\|\Phi\| \leq \overline{\Phi} \triangleq \|G\|M_Q + \|\overline{\nu}\|$. As in [18], if there exists a class $\mathcal{KL}$ function $\beta(\cdot,\cdot)$ and a class $\mathcal{K}$ function $\gamma(\cdot)$, which is called a gain function, such that for any input $\dot{Q}(\cdot) \in L_\infty^m$ and any $\tilde{x}(0)$

$$\|\tilde{x}(t)\| \leq \beta(\|\tilde{x}(0)\|, t) + \gamma(\|\dot{Q}(\cdot)\|_\infty) \tag{26}$$

then the system (25) is said to be ISS.

Consider the Lyapunov function candidate

$$V_1 = \tilde{x}^\top \tilde{x} = \|\tilde{x}\|^2 \tag{27}$$

The derivative of V is

$$\begin{aligned}\dot{V}_1 &= \dot{\tilde{x}}^\top \tilde{x} + \tilde{x}^\top \dot{\tilde{x}} \\ &= [(A-LC)\tilde{x} + \Phi - Ln]^\top \tilde{x} + \tilde{x}^\top [(A-LC)\tilde{x} + \Phi - Ln] \\ &= \tilde{x}^\top [(A - LC)^\top + (A - LC)]\tilde{x} + 2\tilde{x}^\top(\Phi - Ln) \\ &\leq -\lambda_{\min}(M)\|\tilde{x}\|^2 + 2\|\tilde{x}\|(\overline{\Phi} + L\overline{n}) \\ &= -\lambda_{\min}(M)V_1 + 2(\overline{\Phi} + L\overline{n})\sqrt{V_1}.\end{aligned} \tag{28}$$

Comparison principle [19] provides the solution to the differential inequality (28)

$$\|\tilde{x}\| \leq \|\tilde{x}(0)\|e^{-\frac{\lambda_{\min}(M)}{2}t} + \frac{2(\overline{\Phi} + L\overline{n})}{\lambda_{\min}(M)}\left[1 - e^{-\frac{\lambda_{\min}(M)}{2}t}\right] \tag{29}$$

where M and $\|\tilde{x}(0)\|$ verify $\lambda_{\min}(M)\|\tilde{x}(0)\| > 2(\overline{\Phi} + L\overline{n})$. To satisfy the ISS condition, let

$$\beta(\|\tilde{x}(0)\|, t) = \|\tilde{x}(0)\|e^{-\frac{\lambda_{\min}(M)}{2}t} \tag{30}$$

$$\gamma(\|\dot{Q}\|_\infty) = \frac{2\overline{\Phi}}{\lambda_{\min}(M)}\left[1 - e^{-\frac{\lambda_{\min}(M)}{2}t}\right] \tag{31}$$

and it is straightforward to show that β is a class $\mathcal{KL}$ function and γ is class $\mathcal{K}$. Hence, we conclude that the system (25) is ISS. In addition, due to the exponentially decaying terms at right-hand side of (29)

$$\|\tilde{x}\| \leq R_b = \frac{2(\overline{\Phi} + L\overline{n})}{\lambda_{\min}(M)} \quad \text{as } t \to \infty. \tag{32}$$

Therefore, with bounded unknown input $\dot{Q}$ and bounded uncertainties ν in thermal dynamics, $\|\tilde{x}\|$ will settle on or within a norm ball of radius R_b in the error space. □

Remark 4: The size of R_b may be reduced by optimally selecting gain L to balance convergence speed and robustness to uncertainty. A large L enlarges the denominator of R_b, but also amplifies the measurement noise in the numerator.

According to [20], we can compute heat generation $\dot{Q}$ by inverting plant model dynamics (7). Nonetheless, we do not know the exact value of states $x(t)$. By using certainty equivalence [21], the unknown input estimate can be obtained by replacing the state $x(t)$ with its estimation $\hat{x}(t)$

$$\widehat{\dot{Q}}(t) = G^\dagger(\dot{\hat{x}}(t) - A\hat{x}(t) - Bu(t)) \tag{33}$$

where $G^\dagger = (G^\top G)^{-1}G^\top$ is the left inverse of G. Heat generation estimation calculated in (33) will be utilized to design observers in Stage 2.

Remark 5: There exists a loop between the two blocks in Stage 1. Specifically, the heat generation estimates are used for thermal parameter identification, and meanwhile the identified thermal parameters alter the system matrix A. Herein, we analyze each block separately, and only verify the stability of the coupling in the simulation.

B. Stage 2: Battery SOC and Capacity Estimation

The Stage 2 simultaneously estimates battery SOC (unmeasured state) and capacity (unknown parameter) by receiving the core temperature and heat generation estimates from Stage 1 as input signals. We consider the following sliding mode observer structure for the Stage 2

$$\dot{\widehat{\mathrm{SOC}}} = L_3 \mathrm{sgn}(\mathrm{OCV}_m - \widehat{\mathrm{OCV}}) \tag{34}$$

$$\mathrm{OCV}_m = \frac{\widehat{\dot{Q}}}{I_m} + V_{T,m} + \widehat{T}\frac{dU}{dT} \tag{35}$$

$$\widehat{T} = \frac{1}{2}(T_{s,m} + \widehat{T}_c) \tag{36}$$

where I_m, $V_{T,m}$, and $T_{s,m}$ are the current, terminal voltage, and surface temperature measurements. Gain L_3 is the scalar observer gain to be designed. $\widehat{\mathrm{OCV}}$ is the OCV estimation corresponds to SOC estimation $\widehat{\mathrm{SOC}}$. Note that $\widehat{\dot{Q}}$ and $\widehat{T}_c$ are the estimated heat generation from (33) and estimated core temperature from (20). As analyzed in the previous section, the $\widehat{\dot{Q}}$ and $\widehat{T}_c$ estimation are biased due to thermal model uncertainties and unknown heat generation. Consequently, OCV_m obtained from (35) is biased. We model the uncertainty between OCV_m and the actual OCV by an additive error term ξ, with $\mathrm{OCV}_m = OCV + \xi$. Note that ξ may also include the measurement noise from I_m and $V_{T,m}$. Under this scenario, we provide the convergence analysis of observer (34)–(36).

Theorem 6: Consider the SOC dynamics (1), estimated heat generation and core temperature from Stage 1. Furthermore, assume OCV is a monotonically increasing function of SOC over domain $0 \leq \text{SOC} \leq 1$. Also, assume bounds $M_I > 0$, $m_{C_{\text{bat}}} > 0$ are known, where $|I(t)| \leq M_I$, $\forall\, t \in \mathbb{R}^+$, $m_{C_{\text{bat}}} \leq C_{\text{bat}}$. If the scalar observer gain L_3 verifies

$$L_3 > \frac{M_I}{m_{C_{\text{bat}}}} \tag{37}$$

then the estimation error $\widetilde{\text{SOC}}(t) = \text{SOC}(t) - \widehat{\text{SOC}}(t)$ from observer (34)–(36) converges to an bounded error ball defined by $|\widetilde{\text{OCV}}| \leq |\xi|$, where $\widetilde{\text{OCV}} = \text{OCV} - \widehat{\text{OCV}}$. Furthermore, estimated battery capacity is given by

$$\widehat{C}_{\text{bat}} = -\frac{I}{L_3 \upsilon} \tag{38}$$

where υ is the filtered version of $\text{sgn}(\text{OCV}_m - \widehat{\text{OCV}})$, computed by passing $\text{sgn}(\text{OCV}_m - \widehat{\text{OCV}})$ through a low-pass filter with unity steady-state gain in real time, i.e., $\upsilon(t) = \{\omega/(s+\omega)\}\text{sgn}(\text{OCV}_m(t) - \widehat{\text{OCV}}(t))$, where ω is the cut-off frequency.

Remark 7: We have assumed that OCV is a monotonically increasing function of SOC over the 0%–100% SOC range. This assumption is verified for most of the popular Li-ion chemistry, e.g., $LiCoO_2$-Graphite and $LiFePO_4$-Graphite [22].

Proof: Under the condition of $|\widetilde{\text{OCV}}| > |\xi|$

$$\text{sgn}(\text{OCV}_m - \widehat{\text{OCV}}) = \text{sgn}(\widetilde{\text{OCV}} + \xi) = \text{sgn}(\widetilde{\text{OCV}}). \tag{39}$$

Strict monotonicity of the OCV–SOC relationship guarantees

$$\text{sgn}(\text{OCV} - \widehat{\text{OCV}}) = \text{sgn}(\text{SOC} - \widehat{\text{SOC}}). \tag{40}$$

Consequently, we can rewrite observer (34) based on (40)

$$\dot{\widehat{\text{SOC}}} = L_3 \text{sgn}(\text{SOC} - \widehat{\text{SOC}}). \tag{41}$$

The dynamics of $\widetilde{\text{SOC}} = \text{SOC} - \widehat{\text{SOC}}$ can be written as

$$\dot{\widetilde{\text{SOC}}} = \dot{\text{SOC}} - \dot{\widehat{\text{SOC}}} = -\frac{I}{C_{\text{bat}}} - L_3 \text{sgn}(\widetilde{\text{SOC}}). \tag{42}$$

We consider the following Lyapunov function candidate:

$$V_3(t) = \frac{1}{2}\widetilde{\text{SOC}}^2 \tag{43}$$

and the derivative of V_3 along the trajectories of $\widetilde{\text{SOC}}$ is

$$\begin{aligned}
\dot{V}_3(t) &= \widetilde{\text{SOC}} \cdot \dot{\widetilde{\text{SOC}}} = \widetilde{\text{SOC}} \left(-\frac{I}{C_{\text{bat}}} - L_3 \text{sgn}(\widetilde{\text{SOC}}) \right) \\
&= -\frac{I}{C_{\text{bat}}} \widetilde{\text{SOC}} - L_3 \text{sgn}(\widetilde{\text{SOC}}) \cdot \widetilde{\text{SOC}} \\
&\leq \frac{|I|}{C_{\text{bat}}} |\widetilde{\text{SOC}}| - L_3 |\widetilde{\text{SOC}}| \\
&= |\widetilde{\text{SOC}}| \cdot \left(\frac{|I|}{C_{\text{bat}}} - L_3 \right).
\end{aligned} \tag{44}$$

Choose the gain L_3 high enough such that $L_3 > M_I / m_{C_{\text{bat}}}$. Furthermore, note from (43) and (44) that

$$\dot{V}_3 \leq -\alpha \sqrt{2 V_3}, \quad \text{where } \alpha = L_3 - \frac{M_I}{m_{C_{\text{bat}}}}. \tag{45}$$

Applying the comparison principle on (45) suggests the finite time for $\widetilde{\text{SOC}}$ to converge to the error ball defined by $|\widetilde{\text{OCV}}| \leq |\xi|$ to be $t_f = (2V_3(0))^{1/2}/\alpha$. Hence, based on the selection of some high gain L_3, $\dot{V}_3$ will decrease until $|\widetilde{\text{OCV}}| > |\xi|$ is violated. At the sliding mode, we have $\widetilde{\text{SOC}} = \varepsilon$, where ε is less than or equal to the size of the SOC error space corresponds to $|\widetilde{\text{OCV}}| < |\xi|$, and $\dot{\widetilde{\text{SOC}}} = 0$. Substituting these expressions in (42) yields

$$\widehat{C}_{\text{bat}} = -\frac{I}{L_3 \upsilon} \tag{46}$$

where $\upsilon(t)$ is the signal produced from low-pass filtering $\text{sgn}(\text{OCV}_m(t) - \widehat{\text{OCV}}(t))$. □

Remark 8: The battery capacity estimation computed from (46) is expected to be biased as a result of the Stage 1 estimation error ξ. Nevertheless, ξ can be reduced by optimally selecting observer gain L, based on Remark 4.

Remark 9: Given that the thermal parameters vary slowly, the lower block in Stage 1 operates on the slow time scale (cycles) while the upper block and the entire Stage 2 evolve on a fast time scale (second).

IV. Benefits of Thermal Model-Based Capacity Estimation

The fundamental difference between the thermal-based and the equivalent circuit-based approach is that the thermal-based scheme estimates capacity, thermal resistance, heat generation, temperature, and SOC without any need of output voltage model and estimates of R_s (internal resistance) and V_c (voltage of R-C pairs). In the equivalent circuit-based SOH estimation, the SOH estimation error stems from the combined errors of capacity and internal resistance estimation. We, hereby, show conceptually how leveraging thermal dynamics enables to isolate away the estimation error of internal resistance. Essentially, we design an observer to estimate OCV using available online measurements.

A. Thermal Model-Based Estimation

Consider the thermal model-based estimation scheme shown in Fig. 1. In Stage 2, we use the estimated heat generation as the feedback signal in the observer. For a given input current profile and measured terminal voltage within a certain cycle, the heat generation estimation is given according to (4)

$$\widehat{\dot{Q}}(t) = I_m(t) \left[\widehat{\text{OCV}}(t) - V_{T,m}(t) - \widehat{T}(t) \frac{dU}{dT} \right]. \tag{47}$$

Subtract (47) from (4), the feedback error signal is given as

$$\widetilde{\dot{Q}}(t) = I(t) \left[\widetilde{\text{OCV}}(t) - \widetilde{T}(t) \frac{dU}{dT} \right]. \tag{48}$$

Assume $\widetilde{T}(t)$ is negligible due to robust temperature estimation in Stage 1, and the feedback error signal becomes

$$\widetilde{\dot{Q}}(t) = I(t) \cdot \widetilde{\text{OCV}}(t) \tag{49}$$

which captures OCV estimation error only, which is, in turn, dependent only on the capacity estimation error.

B. Electrical Model-Based Estimation

In this case, we use terminal voltage as the feedback signal. Consequently, the feedback error signal is given as

$$\widetilde{V}_T(t) = \widetilde{\mathrm{OCV}}(t) - \widetilde{V}_c(t) - I(t)\widetilde{R}_s \tag{50}$$

where $\widetilde{V}_T$, $\widetilde{V}_c$, and $\widetilde{R}_s$ are the estimation errors for the terminal voltage, voltage across R-C pairs, and the internal resistance. Under this scenario, the estimation errors for capacity ($\widetilde{\mathrm{OCV}}$) and internal resistance ($\widetilde{R}_s$) both emerge.

Methods that estimate capacity and internal resistance from an equivalent circuit perspective, see [6], need crucial assumptions, e.g., linearly varying capacity and internal resistance with respect to time, to distinguish the estimation errors of capacity and internal resistance. However, the thermal-based estimation completely decouples capacity estimation error from the combined SOH estimation error without requiring any such restrictive conditions.

Moreover, though the primary objective for this paper is real-time battery charging capacity estimation, the algorithm presented in this paper can be considered as a novel methodology for combined SOC/SOH estimation. Specifically, it provides estimates for SOC and charge capacity. Even more, Stage 1 produces estimates for thermal model parameters, core temperature, and internal heat generation. To the best of the authors' knowledge, this is the first estimation framework in the literature to estimate all the aforementioned states and parameters simultaneously, with provable convergence properties, under suitable conditions.

V. Results and Discussion

In this section, we present studies on simulation and experiments to validate the performance of the proposed capacity estimation scheme. The battery under test is a LFP A123 26650 cell with an initial capacity of 2.3 Ah.

A. Simulation Study

This section presents the simulation study. The parameter values for thermal model (2) and (3) are taken from [16]. To illustrate the performance, we apply a driving cycle to the battery model. Fig. 2 plots the evolution of current and terminal voltage from the plant model simulation. The estimates (unknown states, input, and parameter) are initialized with incorrect values to illustrate the convergence properties.

We first evaluate the performance of observer (20), (21), and (33) in Stage 1. The core temperature estimate is initialized with 3 °C error. Fig. 3 portrays the evolution of the unknown state (T_c) and unknown input ($\dot{Q}$) from the simulation of thermal system (2) and (3), with their estimated values. Note that with an appropriate choice of observer gain L as presented in Theorem 3, $\widehat{T}_c$ and $\widehat{\dot{Q}}$ converge rapidly. Similarly, the effectiveness of SOC and capacity (C_{bat}) estimation are investigated by initializing SOC estimate with 15% initial error. These results in Fig. 3 confirm the finite-time convergence analysis conclusions for the Stage 2 observers in Section III-B.

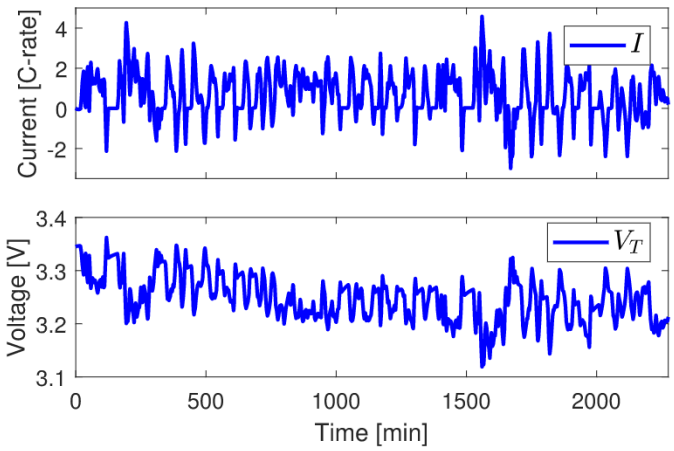

Fig. 2. Simulation of current and terminal voltage in the plant.

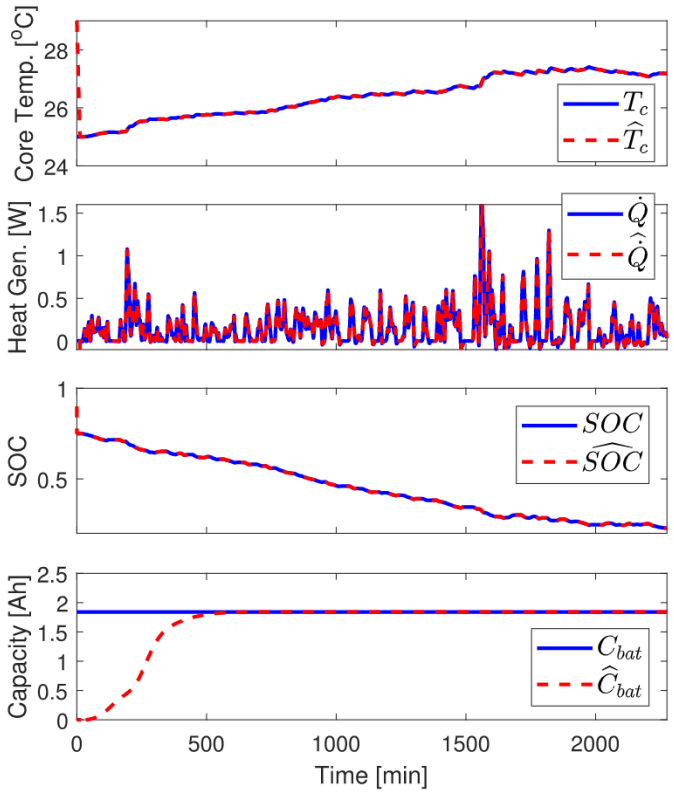

Fig. 3. Estimation performance for the charge–discharge cycle in simulation study, for core temperature, heat generation, SOC, and capacity.

B. Experimental Studies

We further demonstrate the proposed algorithm on experimentally obtained capacity data. The battery cell was placed inside of an ESPEC BTL-433 environmental chamber that maintains the ambient temperature at 25.5^{o}C (298.65 K). A thermocouple was attached to the surface of the cell to measure surface temperature. A PEC SBT2050 cycler was used to apply a repeated charge–discharge cycle (a charging protocol based on the SPMeT model—[23, Fig. 10]) to the battery cell to induce aging (see Fig. 4). The effect of battery aging on terminal voltage and surface temperature is noticeable, especially toward the final 50 cycles, where the cell experiences higher voltage and temperature changes for the same input.

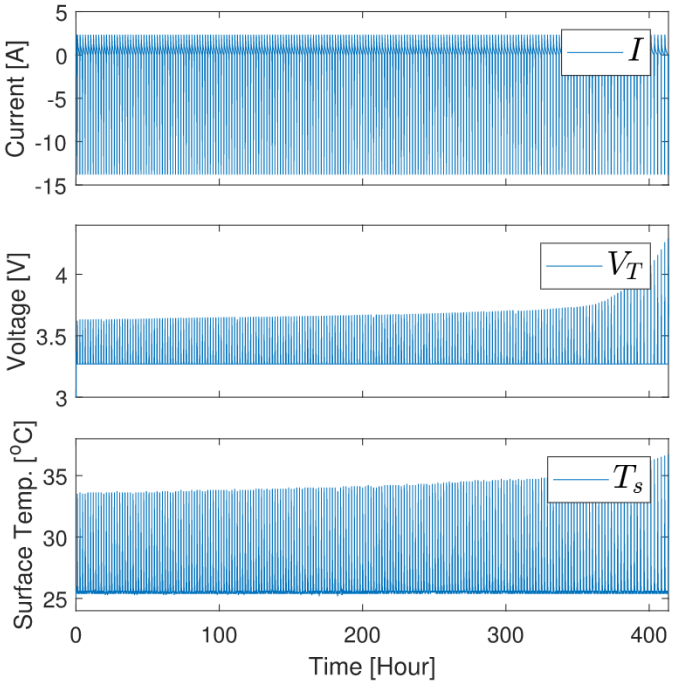

Fig. 4. Experimental data of a repeated charge–discharge profile for 210 cycles, including measurements of input current (I), output terminal voltage (V_T), and surface temperature (T_s).

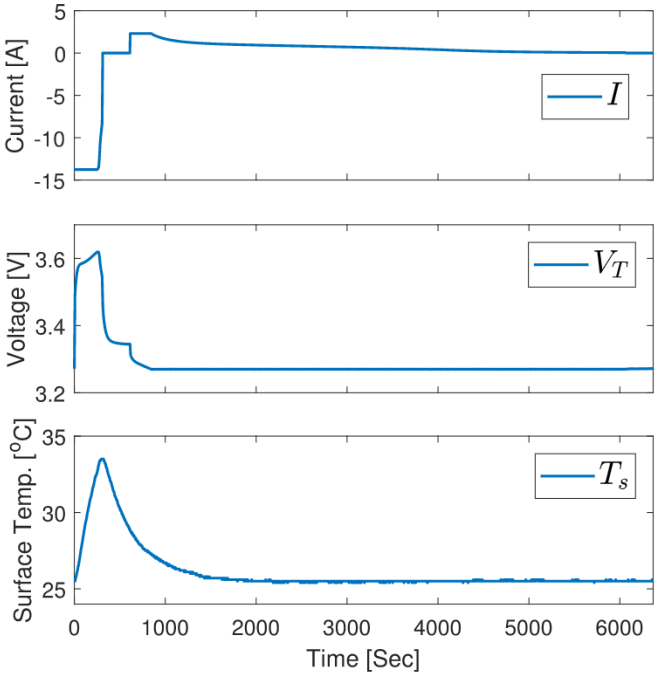

Fig. 5. First cycle of the charge–discharge profile.

Fig. 5 shows the charge–discharge profile for the first cycle, along with the measured voltage (V_T) and surface temperature (T_s). The cell is first charged under $I_{\max} = 6C$ constant current (CC) for 300 s which elevates SOC from initial value 25% to final value 75%, followed by a 300-s resting period ($I = 0$). In the discharge phase, the current initially holds constant but eventually decays over time, resulting in a constant voltage (CV) discharge. The capacity was determined using a 1C CC-CV cycling test at cycle numbers {0, 10, 60, 110, 160, 210}. For real-time implementation, accurate parameter estimation in the thermal model plays a critical role in capacity estimation, due to the flat region of OCV-SOC curve.

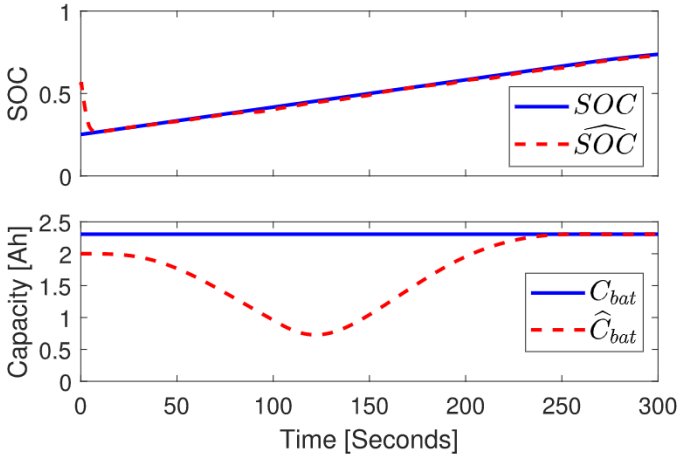

Fig. 6. Evolution of true/estimated SOC and battery capacity (C_{bat}) for the charge period of the first charge–discharge cycle.

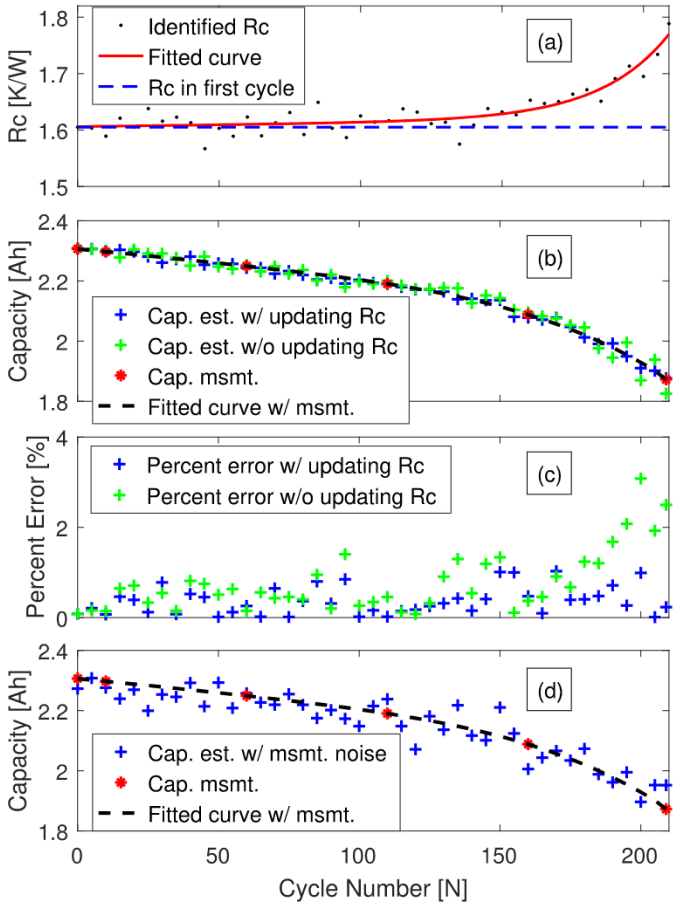

Fig. 7. Battery capacity estimation results, plotted every five cycles. (a) evolution of R_c, and (b) and (c) more accurate estimation with updating R_c in real time. (d) observer robustness against the measurement noise.

Here, we demonstrate the estimation performance for the first charge–discharge cycle. The SOC estimate is initialized with 30% error and capacity estimate is initialized with 0.3 Ah (13%) error. Fig. 6 presents the convergence of SOC

and capacity estimates to their true values. The blue solid line in Fig. 6 (top) represents the evolution of SOC generated by the coulombic counting method. The value of measured battery capacity is 2.31 Ah.

Finally, we examine the capacity estimation performance across 210 cycles under two scenarios.

1) Effect of Updating R_c in Real Time: Fig. 7(a) plots the values of R_c every five cycles as black dots. In spite of the apparent uncertainties stemming from the noisy experimental measurements, the trend of R_c over cycles bears accelerated growth behavior, especially toward the end of the experiments. The frequency for updating R_c (every five cycles) is somewhat arbitrary, but it is selected to adequately track the change rate. We explicitly evaluate the estimation results by comparing two cases: 1) when R_c is updated online and 2) when R_c remains at the value from the first cycle throughout the experiments. Specifically, in Fig. 7(b), the blue and green plus symbols ('+') represent the estimated capacities from case 1) and case 2). Moreover, the red star symbols ('*') are the six capacity measurements, and the black dotted line is the fit curve using the measured data. Note that both cases follow the black curve closely until R_c starts to deviate. Ultimately, after cycle 180, the estimation from case 2) without R_c being updated reveals relatively larger error. The same observation can be made in Fig. 7(c) where the percentage errors of capacity estimation from both cases against the experimentally fitted values are plotted.

2) Effect of Measurement Uncertainties: Despite the fact that the cycled data are experimentally collected, the measurement signals are almost noise free. In order to mimic the real-world applications, a 2% random error is manually added to the signals from Fig. 4 to validate the robustness of the estimation scheme. One may clearly observe from Fig. 7(d) that the capacity estimation result indeed suffers from errors. According to Remark 4, the observer gain L is supposed to be selected to appropriately balance the convergence rate and robustness to measurement noise to minimize the size of R_b. Here, the maximum percentage error between the estimates and the fitted capacity curve is 4.7%.

VI. Conclusion

This paper rigorously analyzes an online capacity estimation scheme for Li-ion batteries from a thermal prospective. Stage 1 estimates core temperature, heat generation, and thermal resistance based on a two-state thermal model, and the second stage receives these estimation signals to estimate SOC and capacity utilizing a sliding mode observer. The convergence for the observers is mathematically analyzed using the Lyapunov stability theory. This approach only requires the tuning of three scalar observer gains, whereas the number of tuning parameters in commonly adopted KF-based methods is polynomial with respect to the number of states. Experimental results demonstrate the capacity estimation accuracy and robustness by comparing with real data. The benefit of using thermal dynamics for capacity estimation is that it decouples capacity estimation error from the combined SOH estimation error.

References

[1] A. Barré, B. Deguilhem, S. Grolleau, M. Gérard, F. Suard, and D. Riu, "A review on lithium-ion battery ageing mechanisms and estimations for automotive applications," *J. Power Sources*, vol. 241, pp. 680–689, Nov. 2013.

[2] C. Weng, J. Sun, and H. Peng, "A unified open-circuit-voltage model of lithium-ion batteries for state-of-charge estimation and state-of-health monitoring," *J. Power Sources*, vol. 258, pp. 228–237, Jul. 2014.

[3] S. Park, A. Savvides, and M. Srivastava, "Battery capacity measurement and analysis using lithium coin cell battery," in *Proc. Int. Symp. Low Power Electron. Design*, 2001, pp. 382–387.

[4] T. F. Fuller, M. Doyle, and J. Newman, "Simulation and optimization of the dual lithium ion insertion cell," *J. Electrochem. Soc.*, vol. 141, no. 1, pp. 1–10, 1994.

[5] G. L. Plett, "Sigma-point Kalman filtering for battery management systems of LiPB-based HEV battery packs: Part 2: Simultaneous state and parameter estimation," *J. Power Sources*, vol. 161, pp. 1369–1384, Oct. 2006.

[6] I.-S. Kim, "A technique for estimating the state of health of lithium batteries through a dual-sliding-mode observer," *IEEE Trans. Power Electron.*, vol. 25, no. 4, pp. 1013–1022, Apr. 2010.

[7] X. Lin *et al.*, "Online parameterization of lumped thermal dynamics in cylindrical lithium ion batteries for core temperature estimation and health monitoring," *IEEE Trans. Control Syst. Technol.*, vol. 21, no. 5, pp. 1745–1755, Sep. 2013.

[8] A. Bartlett, J. Marcicki, S. Onori, G. Rizzoni, X. G. Yang, and T. Miller, "Electrochemical model-based state of charge and capacity estimation for a composite electrode lithium-ion battery," *IEEE Trans. Control Syst. Technol.*, vol. 24, no. 2, pp. 384–399, Mar. 2016.

[9] S. J. Moura, N. A. Chaturvedi, and M. Krstić, "Adaptive partial differential equation observer for battery state-of-charge/state-of-health estimation via an electrochemical model," *J. Dyn. Syst., Meas., Control*, vol. 136, no. 1, p. 011015, 2014.

[10] Y. Xing, E. W. M. Ma, K.-L. Tsui, and M. Pecht, "An ensemble model for predicting the remaining useful performance of lithium-ion batteries," *Microelectron. Rel.*, vol. 53, pp. 811–820, Jun. 2013.

[11] M. Orchard, L. Tang, B. Saha, K. Goebel, and G. Vachtsevanos, "Risk-sensitive particle-filtering-based prognosis framework for estimation of remaining useful life in energy storage devices," *Stud. Inform. Control*, vol. 19, no. 3, pp. 209–218, 2010.

[12] V. Klass, M. Behm, and G. Lindbergh, "Evaluating real-life performance of lithium-ion battery packs in electric vehicles," *J. Electrochem. Soc.*, vol. 159, no. 11, pp. A1856–A1860, 2012.

[13] D. Zhang, S. Dey, H. E. Perez, and S. J. Moura, "Remaining useful life estimation of lithium-ion batteries based on thermal dynamics," in *Proc. Amer. Control Conf. (ACC)*, May 2017, pp. 4042–4047.

[14] C. Park and A. K. Jaura, "Dynamic thermal model of Li-ion battery for predictive behavior in hybrid and fuel cell vehicles," SAE Tech. Paper 2003-01-2286, 2003.

[15] C. Forgez, D. V. Do, G. Friedrich, M. Morcrette, and C. Delacourt, "Thermal modeling of a cylindrical $LiFePO_4$/graphite lithium-ion battery," *J. Power Sources*, vol. 195, no. 9, pp. 2961–2968, 2010.

[16] X. Lin *et al.*, "A lumped-parameter electro-thermal model for cylindrical batteries," *J. Power Sources*, vol. 257, pp. 1–11, Jul. 2014.

[17] B. F. Lund and B. A. Foss, "Parameter ranking by orthogonalization—Applied to nonlinear mechanistic models," *Automatica*, vol. 44, no. 1, pp. 278–281, 2008.

[18] A. Isidori, *Nonlinear Control Systems*. New York, NY, USA: Springer, 2013.

[19] H. K. Khalil, *Noninear Systems*. Upper Saddle River, NJ, USA: Prentice-Hall, 1996.

[20] B. Shafai and M. Saif, "Proportional-integral observer in robust control, fault detection, and decentralized control of dynamic systems," in *Control and Systems Engineering*. Cham, Switzerland: Springer, 2015, pp. 13–43.

[21] P. A. Ioannou and J. Sun, *Robust Adaptive Control*. Chelmsford, MA, USA: Courier Corporation, 2012.

[22] M. Safari and C. Delacourt, "Modeling of a commercial graphite/$LiFePO_4$ cell," *J. Electrochem. Soc.*, vol. 158, no. 5, pp. A562–A571, 2011.

[23] H. E. Perez, S. Dey, X. Hu, and S. J. Moura, "Optimal charging of Li-ion batteries via a single particle model with electrolyte and thermal dynamics," *J. Electrochem. Soc.*, vol. 164, no. 7, pp. A1–A9, 2017.

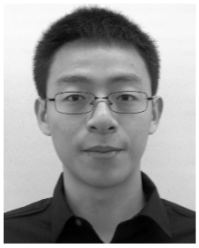

Dong Zhang received the B.S. degree in civil and environmental engineering from the University of Michigan, Ann Arbor, MI, USA, in 2015, the B.S. degree in electrical and computer engineering from Shanghai Jiao Tong University, Shanghai, China, in 2015, and the M.S. degree from the University of California at Berkeley, Berkeley, CA, USA, in 2016, where he is currently pursuing the Ph.D. degree.

His current research interests include energy systems, battery management system designs, estimation and control for nonlinear and infinite-dimensional dynamical systems.

Mr. Zhang has been nominated for the Energy Systems Best Student Paper Award at the 2018 IEEE American Control Conference.

Satadru Dey received the master's degree in control systems from IIT Kharagpur, Kharagpur, India, in 2010, and the Ph.D. degree in automotive engineering from Clemson University, SC, USA, in 2015.

He was a Post-Doctoral Researcher at the University of California at Berkeley, Berkeley, CA, USA, from 2015 to 2017. From 2010 to 2012, he was with General Electric Company as a Control Engineer. He is currently an Assistant Professor of electrical engineering with the University of Colorado Denver, Denver, CO, USA. His technical background is in the areas of controls in energy and transportation systems. His current research interests lie in energy and transportation systems. He is currently focusing on developing control, estimation, and diagnostics algorithms for batteries, ultracapacitors, fuel cells, electric vehicles, and connected and autonomous vehicles.

Hector E. Perez (S'14–M'17) received the B.S. degree in mechanical engineering from California State University, Northridge, CA, USA, in 2010, the M.S.E. degree in mechanical engineering from the University of Michigan, Ann Arbor, MI, USA, in 2012, and the Ph.D. degree in systems engineering from the University of California at Berkeley, Berkeley, CA, USA, in 2016.

He is currently a Post-Doctoral Researcher with the University of California at Berkeley. His current research interests include modeling, estimation, optimal control, and the experimental validation of energy systems.

Dr. Perez was a recipient of the Ford Foundation Pre-Doctoral and GEM Fellowships. He was also a recipient of the AACC O. Hugo Shuck Best Paper Award, the ACC Best Student Paper Award, the ASME DSCC Energy Systems Best Paper Award, and the ASME DSCC Best Paper Award from the Renewable Energy Systems Session.

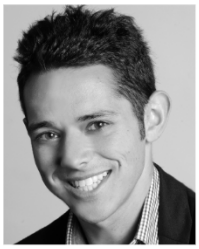

Scott J. Moura (S'09–M'13) received the B.S. degree from the University of California at Berkeley, Berkeley, CA, USA, and the M.S. and Ph.D. degrees from the University of Michigan, Ann Arbor, MI, USA, in 2006, 2008, and 2011, respectively, all in mechanical engineering.

From 2011 to 2013, he was a Post-Doctoral Fellow with the Cymer Center for Control Systems and Dynamics, University of California at San Diego, San Diego, CA, USA. In 2013, he was a Visiting Researcher at the Centre Automatique et Systems, Mines ParisTech, Paris, France. He is currently an Assistant Professor and Director of the Energy, Controls, and Applications Laboratory (eCAL) in Civil & Environmental Engineering at the University of California at Berkeley. He is also an Assistant Professor with the Smart Grid and Renewable Energy Laboratory, Tsinghua–Berkeley Shenzhen Institute, Shenzhen, China. His current research interests include control, optimization, and machine learning for batteries, electrified vehicles, and distributed energy resources.

Dr. Moura was a recipient of the National Science Foundation Graduate Research Fellowship, the UC Presidential Post-Doctoral Fellowship, the O. Hugo Shuck Best Paper Award, the ACC Best Student Paper Award (as an advisor), the ACC and ASME Dynamic Systems and Control Conference Best Student Paper Finalist (as a student), the Hellman Fellows Fund, the University of Michigan Distinguished ProQuest Dissertation Honorable Mention, the University of Michigan Rackham Merit Fellowship, and the College of Engineering Distinguished Leadership Award.